







ControlPULPlet: A Flexible Real-time Multi-core RISC-V Controller for 2.5D Systems-in-package

Alessandro Ottaviano , *Student Member, IEEE*, Robert Balas , *Student Member, IEEE*, Tim Fischer , *Student Member, IEEE*, Thomas Benz , *Student Member, IEEE*, Andrea Bartolini , *Member, IEEE*, Luca Benini , *Fellow, IEEE*

Abstract—The growing complexity of real-time control algorithms with increasing performance demands, along with the shift to 2.5D technology, drive the need for scalable controllers to manage chiplets’ coupled operation in 2.5D systems-in-package. These controllers must offer real-time computing capabilities, as well as System-in-package (SiP) compatible IO interfaces for communicating with the controlled dies. Due to real-time constraints, a key challenge is minimizing the performance penalty of die-to-die communication with respect to native on-chip control interfaces. We address this challenge with ControlPULPlet, an open-source, real-time multi-core RISC-V controller designed specifically for SiP integration. ControlPULPlet features a 32-bit CV32RT core for fast interrupt handling and a specialized direct memory access engine to automate periodic sensor readout. A tightly-coupled programmable multi-core cluster for acceleration of advanced control algorithms is integrated through a dedicated AXI4 port. A flexible AXI4-compatible die-to-die (D2D) link enables efficient communication in 2.5D SiPs. We implemented and fabricated ControlPULPlet as a silicon demonstrator called Kairos in TSMC’s 65nm CMOS. Kairos runs model predictive control algorithms at up to 290 MHz in a 30 mW power envelope. The D2D link attains a peak duplex transfer rate of 51 Gb/s at 200 MHz, at the minimal costs of just 7.6 kGE in PHY area per channel, adding just 2.9% to the total system area.

Index Terms—Real-time, autonomous control, 2.5D, chiplet, RISC-V

I. INTRODUCTION

An increasing number of integrated systems rely on closed-loop control to meet their mission objectives in terms of performance, power consumption, and thermal stability. The control loop consists of three main components, depicted in Fig. 1. First, sensory circuits on the left side probe the current state of the system. Next, a control policy minimizes tracking errors while maintaining stability by closely following the setpoint of an objective function. Finally, the resulting control actions are applied to physical actuators on the right side, leading to changes in the controlled system’s behavior and, therefore, perturbations within its environment. Since the environment state evolves independently of the control pipeline, it is periodically

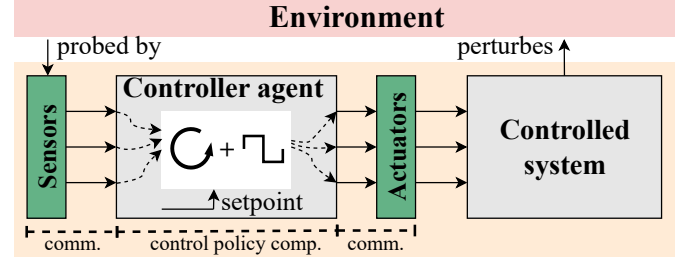


Fig. 1: Main elements involved in the control loop pipeline of a controller agent.

probed by the sensory circuitry. Smaller sampling periods lead to finer granularity of control actions. Such control systems are used across various application domains, including automotive systems and robotics [1], power conversion [2], and CPU power management [3], [4]. For instance, in a smart power converter, the objective function may be conversion efficiency, while in CPU power management, it could correspond to a power budget based on runtime workload and temperature.

The system component executing the control schemes is the controller agent, or controller. To maximize flexibility, controllers are implemented as embedded, Multiple-Input Multiple-Output (MIMO) digital programmable units (see Section IV), with power envelopes from tens to hundreds of mW and on-chip memory footprint under a few MiB [3], [5].

As shown in Fig. 1, a controller performs two main tasks: data communication during sensor readout and actuator configuration, and processing for control policy computation. These tasks are constrained by three key factors: predictability of execution, real-time performance, and reliability. This work focuses on the first two properties. Predictable and real-time execution means the communication and processing pipelines must complete deterministically before the next control loop period begins, known as the deadline. To achieve this goal, we need to meet three design objectives: (1) designing controllers with predictable hardware features, such as cache-less memory hierarchies using scratchpad memories (SPMs) or simple, in-order, non-speculative processor cores; (2) ensuring physical isolation between the controller and its environment to reduce interference on shared resources, such as the interconnect (bus) hierarchy. Isolation includes runtime freedom from interference, fabrication-level independence, and standalone certification for safety integrity [6]; (3) minimizing communication and processing latency. Communication latency can

A. Ottaviano, and R. Balas contributed equally to this work.

A. Ottaviano, R. Balas, T. Fischer, T. Benz, and L. Benini are with the Integrated Systems Laboratory (IIS), ETH Zurich, Switzerland. E-mail: {aottaviano, balasr, tbenz, fischeti, lbenini}@iis.ee.ethz.ch

L. Benini is also with the Department of Electrical, Electronic and Information Engineering (DEI), University of Bologna, Bologna, Italy.

A. Bartolini is with the Department of Electrical, Electronic and Information Engineering (DEI), University of Bologna, Bologna, Italy. E-mail: a.bartolini@unibo.it

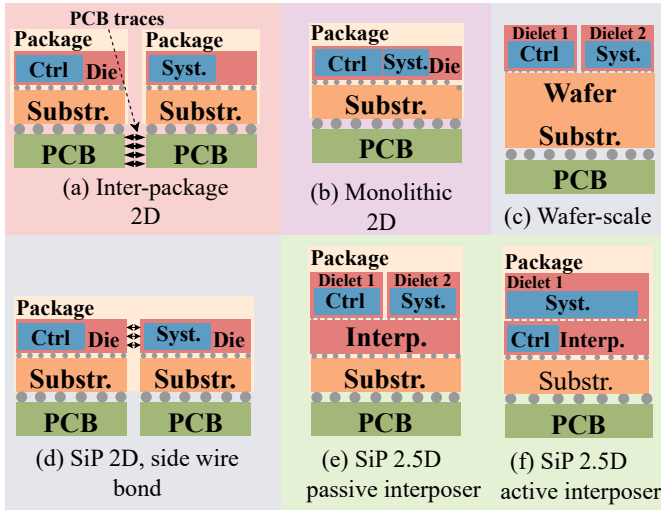


Fig. 2: Controller topologies, categorized by packaging technology.

be reduced through high-bandwidth interfaces between the controller and the controlled system, and through fast interrupt response times (< 10 clock cycles). Processing latency can be improved by scaling the controller’s computing resources (e.g., domain-specific accelerators (DSAs) or multi-core architectures) tailored to the complexity of the control policy.

Another impacting factor on the isolation and communication latency is the integration strategy of the controller and the controlled system, which we depict in Fig. 2. Inter-package integration (Fig. 2a) offers excellent isolation but higher communication latency. Conversely, monolithic integration on the same silicon die (Fig. 2b) minimizes latency but hinders isolation, as components share resources during operation and are logically indivisible as part of the same fabrication process.

Systems in package (SiPs) offer a tradeoff between isolation and latency by enclosing multiple chips in a single carrier. In this setup, die-to-die (D2D) connections between the controller and the system can be implemented using wire bonding (Fig. 2d), as seen in commercial Si-GaN power switches [7]. The latest development in system in package (SiP) technology is the “disintegration” of a monolithic silicon die in many chipselets, or dielets. This post-Moore approach reduces design and production costs, improves production yield thanks to smaller chip sizes, and facilitates the integration of heterogeneous components fabricated independently [8]. Passive or active interposers hosting D2D connectivity fabrics [9] offer up to $44\times$ the bandwidth of off-chip links [10], though still lower than native on-die communication. Figure 2e-f show an example of controller integration with passive and active interposers, respectively. Beyond interposer technology, bleeding-edge technologies like wafer-scale integration enable dense, low-latency chiplet communication via redistribution layers or silicon bridges on wafer, bypassing traditional packaging, as shown in Fig. 2c.

Early adopters of chiplet technology in commercial products, such as AMD, have leveraged it in high performance computing (HPC) systems and data-intensive machine learning (ML) workloads to address the longer development cycles and

increased expenses of transitioning to advanced manufacturing nodes in conventional monolithic integration [11]–[13]. Recently, chiplets have been explored and prototyped in other domains, e.g., Si-GaN switches, to achieve tighter integration between controllers and controlled systems [2].

Most embedded controllers with real-time and predictable execution requirements continue to rely on monolithic integration. However, as advanced autonomous systems — such as humanoid robots and self-driving cars — demand growing computational performance and integration, while maintaining real-time constraints, they are beginning to face similar challenges to high-performance systems, making SiP approaches for control integration a compelling alternative.

In light of these opportunities and challenges, we present ControlPULPlet, a platform that can be configured for monolithic or SiP integration. The platform builds on the RISC-V ControlPULP controller architecture, which follows the programmable multi-core accelerator (PMCA) paradigm [3]. This paper introduces several hardware enhancements compared to the ControlPULP architecture towards a flexible, real-time embedded controller with 2.5D interface compatibility: (i) it introduces a D2D control interface that can be used as a drop-in alternative to the native AXI4 interface for connecting to the controlled system, facilitating integration in chiplet designs; (ii) it extends the general-purpose core functionality with fast interrupt handling through a lightweight ISA extension, essential in real-time systems, and a specialized, autonomous direct memory access (DMA) engine for periodic data acquisition through the D2D link without any periodic intervention of the processor; (iii) finally, it evaluates these additional features on a silicon demonstrator chip, called Kairos. The synthesizable hardware description is open-source under a liberal license¹.

This paper makes the following contributions:

- An open-source, embedded RISC-V controller with comprehensive real-time and computing capabilities compatible with the monolithic and chiplet design paradigms. The design enhances the open-source ControlPULP [3], tuned for on-chip control applications (Section II).
- A scalable, AXI4-compatible source-synchronous digital D2D link. With eight channels and a flow control buffer depth of 128, the link achieves an average peak bus utilization of 85%, compared to 95% for its on-chip equivalent (Section III-A). This setup incurs a minimal PHY area overhead of 2.9% and results in a negligible performance impact to the latency of an exemplary control loop application (Section III-B). Increasing the buffer depth enhances utilization and matches on-chip control performance, albeit at additional area cost.
- Integration of hardware enhancements for real-time execution: fast interrupt handling and context switching [14], and direct memory access (DMA) with periodic mid-end [15] (Section II-B).
- A standalone, single-core demonstrator chip called Kairos, fabricated in TSMC’s 65 nm node. At 1.2 V, Kairos achieves a peak clock frequency of 290 MHz with a power envelope not exceeding 30 mW during data-

¹<https://github.com/pulp-platform/control-pulp/>

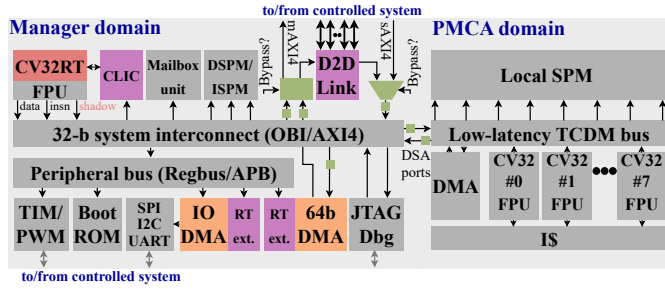


Fig. 3: ControlPULPet architecture, building upon the work in [3]. Extensions introduced in this work are highlighted in color, with pre-existing architectural blocks shown in grayscale for distinction. ■ represents a bus adapter that convert between open bus interface (OBI) and AXI4 protocols, and between 32 b and 64 b bus widths.

intensive control workloads (Section III). On the chip, the D2D link attains a duplex peak transfer rate of 51.2 Gb/s at the nominal 200 MHz (Section III).

II. ARCHITECTURE

In this section, we first describe the ControlPULPet platform, highlighting the main enhancements compared to the ControlPULP architecture (Section II-A). Then, we dive into the integration of the real-time features (Section II-B) and the architecture of the D2D link (Section II-C).

A. ControlPULPet Platform

The high-level block diagram of the ControlPULPet controller is illustrated in Fig. 3. Pre-existing architectural blocks are represented in grayscale, while architectural additions introduced in this work are highlighted with a distinct color scheme for clarity and differentiation.

Manager and programmable multi-core accelerator (PMCA) Domains: The design is centered around a 32-bit, RISC-V manager domain integrating a CV32RT in-order core [14]. To accelerate compute-intensive control workloads, such as model predictive control (MPC), an 8-core, DMA-capable PMCA with per-core 32 b floating point units (FPUs) connects to the manager domain; the PMCA has been extensively validated in [3]. Communication between these domains occurs via two 64 b AXI4 DSA ports, shown in Fig. 3. These ports can be disabled at design time for simpler applications where a single core suffices.

Interconnect System: The interconnect fabric consists of 32 b data and address-wide, 2-clock-cycle access latency, OBI-compliant network elements for low and predictable access latency to the memory system. To bridge with the on-chip and inter-chiplet IO interface, detailed below, the 32 b OBI-compliant data interface is converted to a 64 b AXI4-compliant interface, and arbitrated by an AXI4 crossbar with 3-clock-cycles latency. Several bus adapters convert between the two protocols, as shown in Fig. 3 by the small green rectangles.

On-chip and Inter-chiplet IO Interface: The subordinate interface of the 64 b AXI4 bus — indicated as sAXI4 in Fig. 3 — is responsible for booting the controller. This can be performed by the controlled system, or a separate, secure hardware root-of-trust.

The manager interface — indicated as mAXI4 in Fig. 3 — realizes the sensing/actuation communication path shown in Fig. 1. It is responsible for sensor readout and dispatch of the quantities produced by the control policy. As illustrated in Fig. 3, a bypass network utilizing AXI4-compatible network switches enables selection between the on-chip AXI4 interface and the D2D protocol for I/O connectivity. This selection occurs at the AXI4 bus level, which serves as the frontend network layer of the D2D link. The detailed microarchitecture of the latter is provided in Section II-C. The two interfaces are mutually exclusive, catering to distinct use cases: native AXI4 facilitates on-chip integration with controlled systems, while the D2D protocol supports chiplet-based integration. Consequently, the bypass configuration is static and must be determined at design time prior to physical implementation.

A 64 b, AXI-compliant system DMA engine connects directly with the outgoing D2D interface to decouple off-chiplet transfers from other tasks running on the manager and PMCA domains. This separation also ensures that high-contention dataplane transfers do not interfere with time-critical control-plane operations [16], [17], which are the primary focus of this work. The AXI4-compliant interface enables high-performance transfers through support for burst transactions and multiple outstanding requests. The DMA engine integrates a hardware extension for autonomous, core-independent data movement, which we detail in Section II-B. To allow also the manager core to interact with the controlled system, an additional AXI4 manager port is arbitrated with the system DMA port (green rectangle in Fig. 3).

Memory System: An on-chip, 512 KiB shared L2 SPM in the manager domain serves as the main exchange point with the PMCA, which owns a private, bank-interleaved 128 KiB L1 SPM. In both domains, the OBI interconnect ensures constant access times to the memory endpoints. To minimize access conflicts between large burst transfers from the system or DSA DMA engines and narrow transfers from the manager core, the L2 SPM banks use an interleaved addressing scheme. The L1 SPM employs a similar scheme to reduce interference among the 8 PMCA cores.

Doorbell-based Mailboxes Messaging: ControlPULPet features a configurable doorbell-based mailbox unit with 64 default mailboxes, enabling real-time communication for dispatching requests, setpoint updates, or control policy constraints. The mailboxes are accessible through the AXI4 subordinate external port from the controlled system. A RISC-V core-local interrupt controller (CLIC) handles incoming interrupt lines from peripherals and the mailbox unit; in the latter case, one interrupt line per mailbox is used.

Off-chip IO Interface: To handle off-chip communication with the controlled system, as in the case of discrete physical actuators like motors, brakes, robotic arms, and voltage regulator modules, ControlPULPet supports a broad set of state-of-the-art (SoA) peripherals. Each IO peripheral is managed by a private, IO DMA, featuring a configurable number of peripherals, defaulting to 32 GPIOs, 1 UART, 12 I2C, and 8 SPI. The DMA core architecture mirrors that used for on-chip or D2D communication, since the unit supports multiple interface protocols and thus enables the same hard-

ware to handle diverse scenarios [15]. The autonomous data transfer extension is also supported for off-chip peripherals. Finally, two 32 b system timers and a PWM timer enable diverse periodic control scenarios, such as motor control.

Programming Model: ControlPULPlet employs a lightweight real-time OS (RTOS)-based programming model, supporting multiple RTOSs. An RTOS manages periodic tasks in firmware via platform timers, essential for control applications. This approach underscores two key aspects. First, it emphasizes fast interrupt handling to optimize context switching on single-core processors (Section II-B). Second, it highlights the benefits of a programmable RISC-V-based controller that balances flexibility and specialization. Such a controller supports standardized RTOSs, making it suitable for diverse safety- and time-critical control applications.

B. Real-time features

We detail the real-time extensions integrated into the ControlPULPlet platform, focusing on the interrupt subsystem and autonomous sensor readout. The final paragraph details their system-level integration.

CV32RT: The CV32RT core achieves exceptional performance for real-time tasks through several architectural innovations tailored for minimizing interrupt latency and context switching time. It integrates a fast interrupt controller based on the Core Local Interrupt Controller (CLIC) RISC-V standard. The CLIC introduces support for vectored interrupts, level-based prioritization, and selective hardware vectoring (SHV), which accelerates both nested and non-nested interrupt scenarios. Additionally, the *fastirq* lightweight ISA extension of the core reduces the interrupt latency and context switching to as low as 6 and 100 fixed clock cycles, respectively, on-par to SoA at low area cost. Therefore, the RTOS overhead is bound to 107 clock cycles for context switch and timer tick setup (1 cycle). *fastirq*'s architecture comprises a dual-banked register file with an integrated FSM that triggers a background, fully hardware-managed context-saving mechanism upon interrupt arrival. A bank switch allows immediate execution of the handler while the prior context is asynchronously stored to memory via a dedicated datapath. The design includes stack pointer adjustment logic and memory access coordination to avoid conflicts, enabling consistent execution even during partial saves. When equal-priority, back-to-back interrupts are fired, *tail-chaining* minimizes redundant context save/restore sequences, preserving only the first save and the final restore.

DMA With Real-time Mid-end: For real-time data acquisition tasks, such as reading sensor arrays with complex and irregular address maps, the system integrates a modular DMA [15]. A dedicated real-time (RT) mid-end manages N-dimensional data transfers with support for highly configurable parameters such as stride, shape, and period, enabling precise control of streaming patterns via software. The mid-end architecture includes a microcoded transfer controller and a programmable sequencer, which orchestrate address generation and handshake logic independently from the data path. This decoupling of control and data planes allows data movement to proceed in parallel with computation, minimizing contention

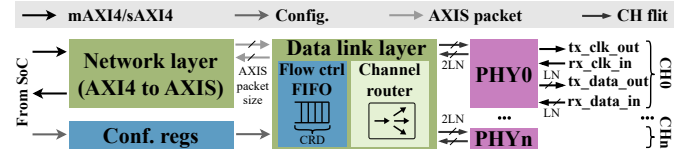


Fig. 4: D2D link architecture overview.

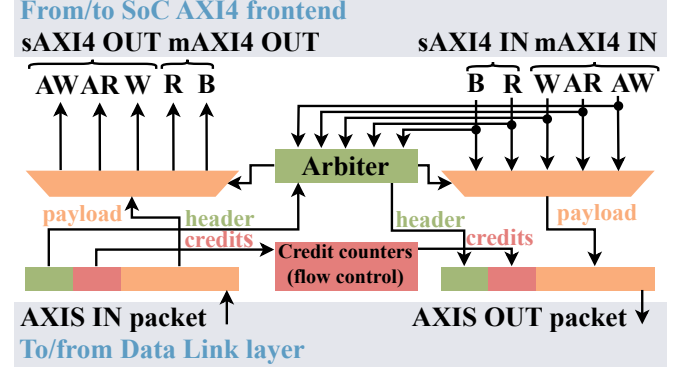


Fig. 5: D2D link network layer.

on shared interconnects and offloading the general-purpose cores. A loop flattening unit and nested loop counter enable complex multidimensional access patterns, while internal FIFOs and backpressure-aware arbitration logic ensure timing-accurate execution in real-time workloads. The autonomous DMA is crucial for maintaining tight timing constraints and preserving computational slack for control algorithms, as discussed in Section III-B.

Integration and Configuration: The CLIC is configured with 128 interrupt lines by default, accommodating 64 interrupts from mailboxes and additional interrupts from other peripherals. To support automatic context saving via the *fastirq* extension, a *shadow* port is injected through the system interconnect from the dual-banked register file. As illustrated in Fig. 3, this port (highlighted in red) handles the saved context, pushed to memory where the stack resides after register banks are swapped upon interrupt reception.

The system DMA engine used for D2D communication is configured with 64 b data width. As shown in Fig. 3, the DMA feeds into the bypass network before selecting the IO protocol of the interface (native AXI4 or D2D link), bypassing the traffic on the main system interconnect to reduce unpredictable delays in the sensor readout path. For off-chip transfers, the IO DMA is configured with 32 b data width, matching the sizing of the APB bus.

C. D2D link

The D2D link is a digital, source-synchronous link employing double data rate (DDR) signaling, designed to translate AXI4 transactions into an off-chiplet interface with a configurable number of channels (*CH*). The channels operate independently, ensuring isolation and flexibility. A channel is composed of a configurable number of data lanes (*LN*), with a source-synchronous clock in each direction. The channels are synchronized at the receiving end of the link. The microarchi-

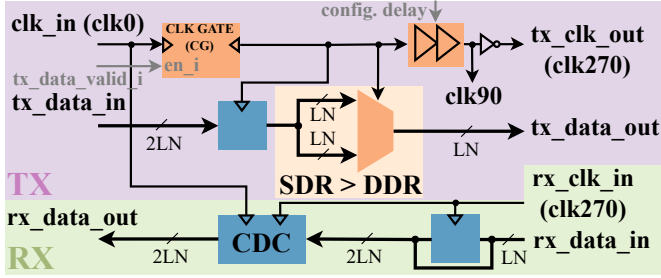


Fig. 6: D2D link PHY for one channel. Highlighted in purple and green are the TX and RX modules, respectively, and their main data and clock signals.

texture of a D2D link is shown in Fig. 4. It implements three layers: **network**, **data**, and **physical (PHY)** layer.

Network Layer: The network layer provides a duplex (manager/subordinate) AXI4 frontend interface. For embedded control chiplets operating on a dedicated control plane, as in our design, AXI4 offers an effective trade-off between simplicity, robustness, and performance, compared to full protocol stacks like PCIe. The network layer serializes duplex AXI4 requests and responses into an AXI stream (AXIS) interface, employing a credit-based flow control mechanism to generate backpressure on the AXI4 frontend.

Figure 5 illustrates the network layer circuitry. The ten channels of the `m_AXI4` and `s_AXI4` ports, as labeled in the figure, are arbitrated based on their transfer direction, thus grouping input/output requests and responses. Flow control is managed through credit counters, which decrement when transactions are issued by the D2D (e.g., address write/read or data write transmissions) and increment when transactions are received by the D2D (e.g., write responses or read requests). This credit-based flow control mechanism generates backpressure on the AXI4 frontend, preventing buffer overflow on the receiver side or guaranteeing no data loss.

For each transfer direction, the network layer converts AXI4 transactions into AXIS packets, multiplexing the five AXI4 channels (AW, W, B, AR, R) into a unified stream (Fig. 5). Each AXIS packet includes: (i) one AXI beat from the selected channel, with a payload width equal to the maximum of all channel widths; (ii) an optional B channel response (used to complete write transactions); (iii) a 4-bit header tagging the AXI channel type; and (iv) a credit count field to support backpressure. The receiver decodes each packet and dispatches the payloads to the appropriate AXI channel. The dataflow of header, payload, and credits in a packet is shown in Fig. 6.

The arbitration policy prioritizes control channels (AR, AW) and follows a round-robin policy to prevent starvation and violation of AXI4 ordering rules [18]. The design does not support transactions issued but not yet completed (out-standing), allowing only one AW/AR transfer with the same transaction ID at a time.

Data Link Layer and Flow Control: The data link layer (Fig. 4) segments the AXIS payload of an AXIS packet into channel-sized flits. When DDR is enabled, each channel has width $2 \cdot \text{LN}$, as shown in Fig. 4 on the right of the Data link layer module, for data transmission and reception, which thereby happens in one clock cycle. This does not account

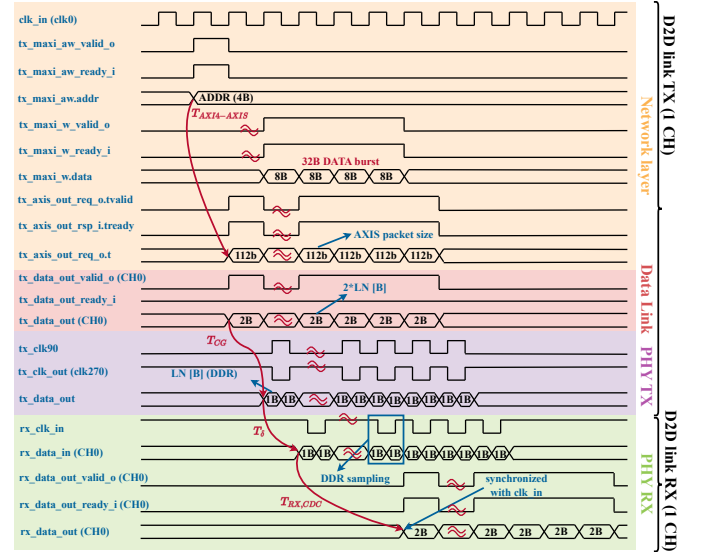


Fig. 7: D2D chronogram of an exemplary 32 B-burst DMA write transfer through the D2D link. We show the network, link, and PHY TX signal interfaces of the transmitting D2D link instance and the PHY RX signal interface of the receiving D2D link instance. Only one channel is shown for readability.

for the transmitting and receiving clocks. In this setting, the number of bits transferable per clock cycle, or the theoretical bandwidth, is expressed as $\theta = 2 \cdot \text{CH} \cdot \text{LN}$ b.

The data link layer includes a flow control credit buffer to store incoming data. This buffer operates as a FIFO (First-In, First-Out) queue. In a given D2D instance, data is pushed into the FIFO during reception and popped out during transmission. A similar process occurs symmetrically in the FIFO queue on the other D2D instance. The network layer's flow control mechanism ensures that the FIFO does not overflow by applying backpressure as needed. To prevent deadlocks during long write/read bursts, e.g. from the system DMA, the network layer can send empty payload packets with credits to match the capacity of the burst transfer.

Each FIFO element has a size of θ , meaning it contains all the data flits across all channels. The FIFO depth equals the number of flow control credits CRD times the number of splits (or chunks) required to divide a packet into smaller segments: $\text{CRD} \cdot (\text{size}(\text{packet}) / \theta)$. One should aim at configuring the link to preserve the original packet size, minimizing the number of chunks, else increasing the FIFO depth. The CRD parameter plays a critical role in determining the link throughput, particularly for large write/read bursts where the FIFO dimensions constrain the backpressure efficiency. This impact is analyzed in detail in Section III-A.

A channel router, shown in Fig. 4, combinationally splits the stream in flits and distributes them across the channels. When $\text{CH} = 1$, the router module is bypassed in hardware to save area. Faulty channel support could be incorporated into the D2D design by extending the data link layer with hardware-level detection and suppression during link calibration. We leave this enhancement to future work.

PHY Layer: The PHY layer of a single channel provides access to the data lanes and the transmitting/receiving

clock signals across all channels. Each channel includes both a transmission (TX) module and a receiver (RX) module, highlighted in Fig. 6 in purple and green, respectively. When DDR signaling is enabled, the channel flit `tx_dat_in`, of size $2 \cdot LN$, is transmitted in one clock cycle. This means that the data interface exposed by the link, of size LN on the transmission and reception paths, sends or receives data every half clock cycle to keep up with the bandwidth supplied by the data link layer flits. At the circuit level, on the TX path, we use a clock multiplexer to alternate the transmission of LN data bits depending on the clock signal's high or low phase, thereby achieving DDR signaling. Alternatively, single data rate (SDR) signaling can be used bypassing the clock multiplexing logic, albeit with a potential reduction in performance.

The TX module forwards a source-synchronous clock, `tx_clk_out`, off-chiplet alongside the channel flit. This forwarded clock incorporates a three-quadrature (270°) phase shift relative to the PHY input clock, `clk_in`, to maximize the data sampling window. The phase shift is achieved using a fully digital, configurable delay line implemented as a binary tree of multiplexers. This structure shifts the clock by 90° , and a cascade inverter is used to achieve the final three-quadrature phase shift, illustrated in Fig. 6. This three-quadrature shifting optimizes the data sampling eye window, enabling robust data transmission. To ensure data is sampled only when valid, the TX module employs a clock gate (CG) cell. The CG is controlled by the `tx_data_valid_i` signal and modulates the logic level of the PHY's source clock prior to phase shifting. The data-valid/ready handshake signals are generated at the data link layer and are derived from their corresponding signals in the AXI4 and AXIS frontends injected at the network layer. On the RX side, data sampling is performed using the received clock, `rx_clk_in`. A FIFO-based clock domain crossing (CDC) with 2-stage flip-flop synchronizers is responsible for synchronizing the incoming data stream, `rx_data_in`, with the PHY source clock `clk_in`. At the circuit level, when DDR is enabled, the `rx_data_in` input of size LN is sampled every cycle on the falling edge of the receiving clock (thus, every half-clock cycle), as illustrated by the flip-flop in the bottom-right corner of Fig. 6. This value is then coalesced with the sample captured on the rising edge of ControlPULP's clock to form a $2 \cdot LN$ -bit data flit over a full clock cycle, fed to the CDC described above. The total number of wires exposed by the PHY is given by $N_{wrs} = CH \cdot (2 \cdot (LN + 1))$, which accounts for the data lanes and the forwarded clock in both input and output directions (duplex).

Latency: Figure 7 illustrates the chronogram of a 32 B burst transfer initiated by the system DMA via a D2D link configured with $LN = 8$ b and $CH = 8$. The diagram showcases the network, link, and TX PHY interfaces of the transmitting D2D instance, along with the RX PHY interface of the receiving instance. Only the first channel of the data link layer and PHY is depicted. The transmitting and receiving instances are interconnected to form the inter-chiplet bridge.

At the network layer (yellow), a 4 B address is first transmitted on the `AW` channel, followed by the 32 B data on the `W` channel. Since the system DMA has a 64 b data width, 8 B are dispatched per clock cycle. The handshake signals associated

with the transfer are also shown. The number of clock cycles between the address and data transmissions depends on the implementation of the DMA and the controller interconnect. For simplicity, this delay is depicted as 1 clock cycle, denoted by the symbol \approx . The AXI4 interface is then converted into an AXIS interface, represented by the tuple `tx_axis_out_req_o.t` and `tx_axis_out_req_o.t_valid`. The latency for this conversion, $T_{AXI4-AXIS}$, is at most 1 clock cycle. The D2D link configuration ensures that the AXIS data payload size fully encapsulates the upstream AXI4 transactions.

At the data link layer (red), the `tx_data_out` payload for a single channel is shown, with each flit being $2 \cdot LN = 2$ B. The handshake interface for the data link layer is also included. The channel flit splitting of the AXIS stream and its subsequent routing incur no additional latency.

The PHY layer illustrates the TX interface of the transmitting D2D link (purple) and the RX interface of the receiving D2D link (green) for one channel. At the PHY TX layer, the `tx_data_out` signal is transmitted on both edges of the transmitted clock (`tx_clk_out`), resulting in a data rate of 1 B per half clock cycle in this example. The PHY TX layer incurs a latency, $T_{RX,CDC}$, of 1 clock cycle due to the clock gating cell, which latches the enable signal at the rising edge of `clk_in` and applies it at the subsequent clock cycle.

Once the data and clock signals leave the PHY TX of the transmitting D2D instance, they are synchronized by the RX module of the receiving D2D instance. The inter-chiplet latency between the two links is determined by the IO, interposer, and packaging solution. This delay is depicted as T_δ in the chronogram and is set arbitrarily to 1 clock cycle for readability. On the receiving PHY (RX PHY), up to three additional clock cycles are required to synchronize the `rx_data_in` signal with `rx_data_out` between `rx_clk_in` and `clk_in` via the CDC. This delay is due to the synchronization and buffer logic within the CDC.

After the PHY RX layer in the receiving D2D instance, the data path (data link and network layer) mirrors that of the transmitter and thus is omitted from Fig. 7.

While the D2D link is not fully latency-insensitive in the theoretical sense, since it relies on finite buffering and timely credit returns, it achieves a high degree of latency tolerance through handshake-based elastic buffering and credit-based flow control. This design absorbs link-level jitter and moderate inter-chiplet delays, as we show in Section III-A.

III. EXPERIMENTAL RESULTS

We first present a functional evaluation of the D2D throughput (Section III-A). Then, we assess and discuss the impact of the D2D interface and real-time features on an exemplary dynamic voltage and frequency scaling (DVFS) control loop case study (Section III-B). Figure 8 illustrates the testbench setup for cycle-accurate RTL simulations, which comprises ControlPULPlet and its D2D link instance, and a destination D2D link instance. The vertical dashed green line shows the chiplet boundary. The destination D2D link connects to a duplex downstream memory controller². This choice is

²Available open-source at <https://github.com/pulp-platform/axi>

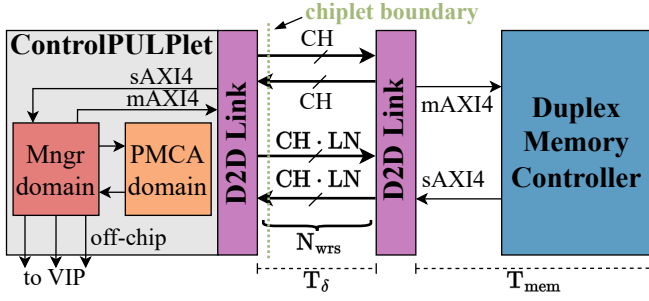


Fig. 8: Simulation setup. The D2D interface of a ControlPULPlet instance is connected to another D2D instance and then to an AXI4 duplex memory controller. The testbench environment uses the register transfer level (RTL) description of the actual hardware; it is, therefore, cycle-accurate.

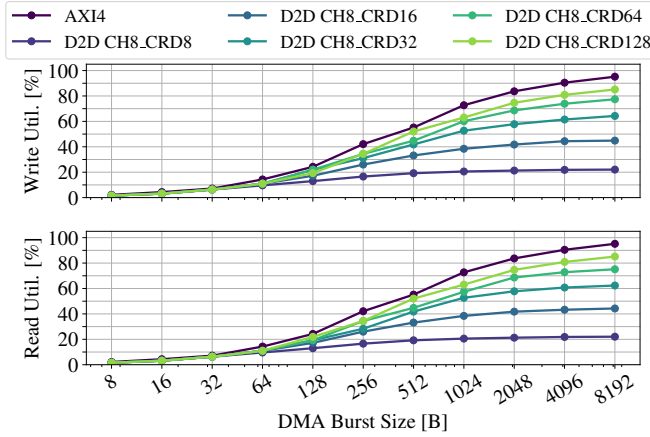


Fig. 9: Throughput comparison between D2D link and AXI4 with $CH = 8$ and $LN = 8$ b at varying CRD and system DMA burst size in bytes.

preferred over a loopback configuration, which would connect ControlPULPlet's D2D link's input and output, as it allows modeling the storage elements of sensors/actuators for the controller policy. The latency of the interconnect and memory system after the receiving D2D instance is represented as T_{mem} . In this simulation setup, both T_δ and T_{mem} are configurable. Figure 8 also highlights ControlPULPlet's off-chip interface, connected to verification IPs (VIPs) to simulate communication along this path.

A. D2D Throughput

Sizing the D2D Link: Finding an optimal D2D link configuration requires determining the minimum values of LN and CH that can sustain the bandwidth of the native AXI4 interface after serialization into the AXIS protocol, namely $\theta \geq$ AXIS packet size. As described in Section II-C, the size of an AXIS packet includes a constant and variable component. The constant component is determined by the system-level configuration of the five AXI channels. It is approximately 100 b for a configuration with 64 b data and 32 b address widths, as for ControlPULPlet's system DMA. The variable component depends on the depth of the control flow FIFO, as credits are sent/received over the D2D interface. When using the native AXI4 interface, the DMA can transfer up to 64 b per clock cycle, i.e. $\theta = 64$ b. To ensure that the D2D link matches

this theoretical bandwidth, a channel width of $CH \geq 7$ and $LN \geq 8$ b guarantees that $\theta \geq 112$ b can be transferred at each clock cycle. For this evaluation, we select an upper bound $CH = 8$ and $LN = 8$ b. This makes the flow control FIFO size dependent on the choice of CRD only. Additionally, we configure $T_\delta = 0$ and $T_{mem} = 1$ clock cycles to minimize external overhead in the throughput evaluation.

Bus Throughput and Utilization: Once the theoretical bandwidth θ is determined, the maximum attainable duplex throughput of the D2D link reads $\Theta = 2 \cdot \alpha \cdot f \cdot \theta$ b/s, where $\alpha \in [0, 1]$ is the relative bus utilization, and f is the operating frequency. At $f = 200$ MHz, this configuration achieves a theoretical bandwidth of $\Theta = \alpha \cdot 51.2$ Gb/s. It represents the bus inefficiencies, i.e., clock cycles wasted without transferring data. In the context of our D2D design, α is influenced by factors including the additional conversion latencies introduced by the AXI4 frontend (Fig. 7) and the limited storage capacity of the flow control FIFO. Consequently, even when θ is carefully selected to match the theoretical bandwidth of the native on-chip AXI4 interface, α inherently reflects the impact of the architectural design choices made for the D2D link, affecting the overall throughput Θ .

Results and Discussion: We measure the D2D link's read and write paths throughput Θ at varying CRD . We compare it with the throughput achieved by the native AXI4 on-chip interface without D2D link. For this purpose, the system DMA is programmed to issue repeated write and read transfers at increasing burst sizes, starting from 8 B.

Results are shown in Fig. 9. The native on-chip interface, labeled as AXI4 and represented in purple, approaches peak utilization ($\alpha = 1$) starting from burst sizes of 2 KiB, the maximum permitted by the AXI4 specifications. The D2D interface achieves approximately 85 % bus saturation for large bursts on the write and read paths with $CRD = 128$, compared to 95 % of the native AXI4 on-chip performance. The performance gap can be narrowed by increasing further the FIFO depth CRD , but results in greater area overhead for the D2D link and may necessitate a different implementation strategy for the flow control buffer, e.g., an SRAM-based design. This area cost is evaluated in-system in Section III-D.

B. Case study: Online DVFS Control Loop of HPC Processors

We consider a control scenario involving online DVFS of HPC processors. In this application, the controlled system includes N_c application-class processing elements (PEs). The sensory layer consists of on-chip Process, Voltage, Temperature (PVT) sensors. The actuation layer includes setting on-chip phase locked loops (PLLs) for per-core frequency scaling and off-chip voltage regulators for voltage scaling. We consider 500 PVT sensor registers of 8 B each. Similarly, we assume one PLL per-core. Setpoints, such as the reference DVFS operating point, are asynchronously sent to the controller via the mailbox unit. The online control policy solves a floating-point MPC problem periodically, which outputs the controlled DVFS points. The MPC uses a prediction horizon $H_p = 2$. For a detailed discussion of the MPC power and thermal model, we refer the reader to [19]. We define the DVFS control problem for each PE as $PN_c \times N_{c_Hp}$.

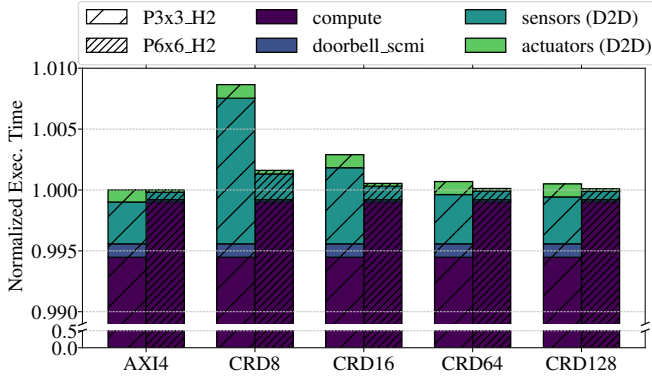


Fig. 10: Impact of D2D communication over native on-chip communication (AXI4) on a DVFS CPU control scenario at a varying number of CRD . $CH = 8$ and $LN = 8$ b for the D2D link.

Evaluation Settings: We configure the RTL testbench setup in Fig. 8 with $T_\delta = 50$ and $T_{\text{mem}} = 100$ clock cycles. We consider this a reasonable upper bound for NoC-based interconnect systems with single-cycle access to on-chip memory [3]. Two synchronous, periodic tasks are initiated by FreeRTOS using the platform’s timers: a task for voltage sensing and actuation through the off-chip interface and a task for temperature sensing, control policy computation, and frequency actuation through the D2D interface. The two tasks have different periods: $T_{\text{short}} = 250 \mu\text{s}$ and $T_{\text{long}} = 3 \text{ms}$, respectively. ControlPULPlet runs at 500 MHz. The control policy computation is handled by the manager core and terminated after 5 iterations; the PMCA is not used, as MPC acceleration is outside this work’s scope. Message dispatching is simulated by issuing messages to ControlPULPlet’s mailbox at the beginning of each period with the target DVFS setpoint.

Overall, meeting the stringent real-time constraints of this application requires close HW/SW co-design. We define slack as the free time available to the controller before the task with the longest period ends. Denoting the computation and communication times required by the controller as $T_{\text{ctrl}} = T_{\text{comp}} + T_{\text{comm}}$, the slack is calculated as $T_{\text{slack}} = T_{\text{long}} - T_{\text{ctrl}}$. To meet the deadline, we must always ensure $T_{\text{slack}} > 0$.

Results and Discussion: We first highlight the benefits of fast interrupt handling and autonomous DMA before focusing on D2D link communication. The time to decode a message dispatched to the mailbox unit is given by:

$$T_{\text{MSG}} = T_{\text{CLIC-to-ISR}} + T_{\text{ISR}} + T_{\text{ISR-to-dec}}$$

where $T_{\text{CLIC-to-ISR}}$ is the time from CLIC acceptance to the first interrupt service routine (ISR) instruction, T_{ISR} is the ISR execution time, and $T_{\text{ISR-to-dec}}$ is the deferred decoding time, kept outside the ISR to reduce its duration, a common real-time programming practice. $T_{\text{CLIC-to-ISR}}$ achieves a 72% speedup (46 to 13 clock cycles) thanks to automatic hardware-based context saving and restore and, reduces the decoding time by 13%. This acceleration is critical when multiple concurrent message requests from various PEs must be processed by the manager domain. As described in Sec. II-B, this situation benefits from tail-chaining optimizations in the CLIC, dramatically reducing interrupt handling time to 8

clock cycles.

For the system DMA, programming incurs a fixed cost of $T_{\text{single,DMAprog}} = 100$ clock cycles, as it happens once during T_{long} . During long inter-chiplet transfers, the automation of this phase provides significant performance gains. For the IO DMA, the benefit is even greater. Programming must occur periodically (T_{short}) and requires a context switch by the running RTOS. :

$$T_{\text{tot,DMAprog}} = (T_{\text{long}}/T_{\text{short}}) \cdot (T_{\text{single,DMAprog}} + T_{\text{ctx_switch}})$$

With RT-DMA, context switches are eliminated, reducing the overhead to $T_{\text{single,DMAprog}}$. For $T_{\text{short}} = 250 \mu\text{s}$ and $T_{\text{long}} = 3 \text{ms}$, this results in a 98% speedup. These optimizations mitigate T_{comm} and enhance deadline completion guarantees.

Finally, Fig. 10 illustrates the impact of the D2D link on control loop performance for two control problems ($P3 \times 3_H2$ and $P6 \times 6_H2$), where *fastirq* and autonomous DMA are always active. The execution time is normalized to the native AXI4 baseline. For both problems, the baseline already meets the deadline, with $T_{\text{slack}} = 86\%$ and $T_{\text{slack}} = 21\%$ for the smaller and larger problems, respectively. The D2D link is configured with $CH = 8$, $LN = 8$, and varying flow control FIFO sizes. We report on message decoding, sensor/actuator communication, and control policy computation. Compared to the baseline, the D2D interface has predictably a higher T_{comm} . For $CRD = 8$, latency increases by $3.1 \times$ and $3.2 \times$ for $P3 \times 3_H2$ and $P6 \times 6_H2$, respectively. A more efficient D2D configuration, i.e., $CRD = 128$, reduces this gap to $1.1 \times$ in both applications, hereby approaching the native AXI4 performance of on-chip control. As shown in Fig. 10, in the analyzed application the compute phase dominates T_{ctrl} , accounting for over 99% of execution time. Consequently, the D2D link penalty on the overall T_{ctrl} is always negligible, i.e., $<0.9\%$ for $CRD = 8$ and $<0.05\%$ for $CRD = 128$. Certainly, if the MPC computation required fetching some of the data from an off-chip memory, the memory traffic over the D2D link would increase, as well as its penalty.

This section shows that the RT-DMA and an optimally designed D2D link enable high-throughput communication without processor intervention, on par with the native on-chip performance. Fast interrupt handling similarly reduces the processor’s response latency and context-switching overhead, allowing it to focus on computation and PMCA offload, if enabled. In the next section, we show that the D2D-based control also comes at a minimal area and energy cost.

C. Silicon demonstrator

We evaluate ControlPULPlet’s area and energy footprint through a silicon demonstrator named *Kairos*, which is designed, implemented, and fabricated using TSMC’s 65 nm node, targeting a 200 MHz system clock in the SS corner at 125°C . Figure 11 shows *Kairos*’s annotated die shot and implementation characteristics. The chip area is 7.2mm^2 , housed in a QFN64 package with nominal core and IO voltages $V_{\text{dd,core}} = 1.2 \text{V}$ and $V_{\text{dd,IO}} = 2.5 \text{V}$, respectively. All of *Kairos*’ external pads are implemented as regular IOs.

We configure *Kairos* without DSA ports due to area constraints, as the PMCA is not the primary focus of this work

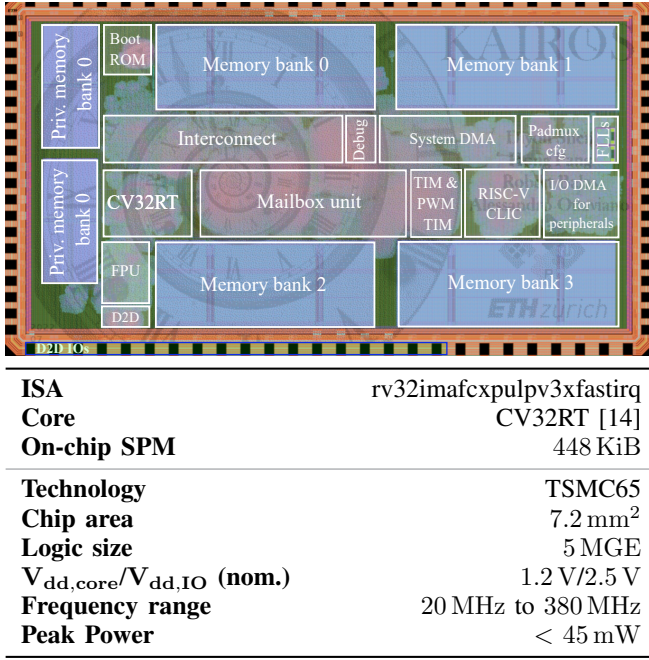


Fig. 11: Annotated die shot of Kairos with key characteristics. We highlight the D2D logic and IOs on the bottom left of the die. The IO pads are on the sides of the chip since the package is quad-flat no-leads (QFN).

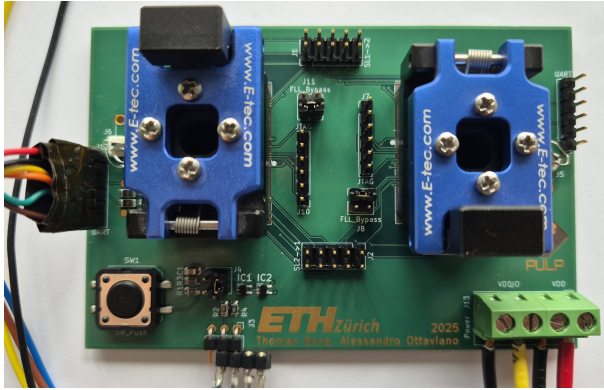


Fig. 12: Kairos evaluation board. Two Kairos chip instances (each in one of the blue sockets) are connected to each other on the PCB through the D2D link. D2D probes are visible on the top and bottom of the figure.

and has already been thoroughly verified in [3]. The manager domain features 448 KiB of SPM to accommodate control firmware components and libraries. The system interconnect configuration defaults to 32 b data and 32 b addresses, while the DMA is configured with a data width of 64 b. The chip integrates one system and PWM timers, one UART, four I2C, four SPI hosts, and 64 mailboxes of 32 B each. We include two on-chip frequency locked loops (FLLs) for the manager and peripheral domain clocks. The D2D link is configured with $CH = 1$ and $LN = 8$, totaling $N_{wrs} = 18$, and $CRD = 8$.

Limitations: We are constrained to a low-performance configuration due to the 64-pin capacity of the surface-mounted, wire-bonded QFN64 package, reflecting practical limitations in accessing advanced 2.5D integration technologies. This limitation constrained the design of the standalone evaluation board for D2D link assessment, which is shown

in Fig. 12. The board integrates two Kairos chips, interconnected to enable communication via their respective D2D links. One chip serves as the controller, the other as a subordinate memory endpoint simulating the controlled system domain. The packaging limitations primarily affect T_δ (see Fig. 7) due to the inter-chip track length, on average 70.5 mm long and 0.2 mm wide in our design compared to the ≈ 1 mm of a native interposer-based design [20]. T_{mem} depends instead on the endpoint of the receiving D2D link, typically the controlled system, and is not affected by the packaging choice. In this implementation, both chips share the same SPM-based memory system with single-cycle access interconnect, bounding T_{mem} to 1–2 clock cycles. An additional limitation arises from the use of a mature technology node, which restricts the minimum operating voltage and keeps the energy-per-bit higher than what advanced nodes could achieve. This partially obscures the performance benefits of our design, particularly the near-lossless interface compared to the monolithic AXI4 counterpart. Despite these limitations, the main D2D link metrics within the chip boundaries (e.g., power, interface energy, and area) remain valid under our simpler off-chip packaging. We detail this evaluation in Section III-D.

D2D Link Scalability and Multi-chiplet Support: This work evaluates the D2D interface using a two-chiplet setup, sufficient to characterize the source-synchronous D2D module in latency, energy, and throughput. Nonetheless, broader scalability and multi-chiplet integration are also relevant, especially for control-centric applications. Two integration models arise in such systems. In a centralized setup, a manager controller chiplet connects to multiple controlled chiplets with distributed sensors/actuators, forming a hub-and-spoke topology. The main controller instantiates multiple AXI4 manager ports and D2D links. ControlPULPlet’s RT-DMA and AXI pipelining allow issuing multiple outstanding transactions in parallel. Since this topology increases area overhead, it underscores the importance of a compact D2D bridge. In the distributed model, each chiplet combines control and sensing/actuation logic, coordinating via D2D links and shared memory (e.g., mailbox or local SPM). The number of D2D ports per chiplet defines the topology, from ring (two) to mesh (four). For control use cases, ring-based topologies are favored due to minimal controller interference.

Adaptability to Advanced Packaging Technologies: Our D2D interface is agnostic to the underlying packaging technology and requires only a routed signal path with controlled impedance and bounded clock skew, constraints that are met by several advanced packaging platforms. In particular, EMIB and Si-IF are well-matched to our D2D design: EMIB provides short silicon bridges with low trace length and skew, ideal for moderate-bandwidth, source-synchronous links; Si-IF offers ultra-dense, low-latency connections, making it especially suitable for tightly coupled chiplets. CoWoS, while offering higher bandwidth and full passive interposers, may exceed the form factor and cost requirements typical of embedded control systems. InFO technologies support compact, low-profile integration for consumer or IoT devices, and our D2D link can be conservatively configured (e.g., fewer channels or reduced frequency) to remain within its timing margins. Overall, the

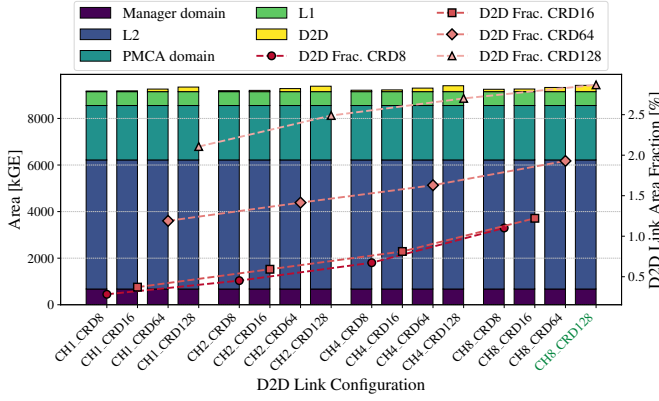


Fig. 13: Impact of D2D link at varying channels and flow control FIFO depth on ControlPULPlet area. LN is fixed at 8 b.

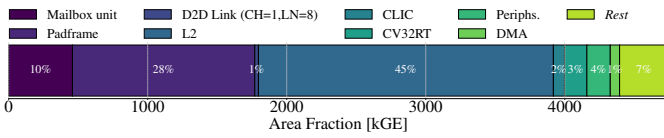


Fig. 14: Kairos area breakdown. Rest denotes the interconnect system, its adapters and other logic.

electrical assumptions of our link are compatible with the wiring models of these platforms, enabling straightforward integration across a range of packaging options.

D. Silicon Performance

We first explore the absolute and relative area impact of the D2D in ControlPULPlet, including the manager and PMCA domains, under various parametrizations using post-synthesis data. Next, we examine the fabricated chip demonstrator configuration (manager domain only), detailing the overall area and energy figures of its key components.

Area breakdown: Figure 13 illustrates the impact of progressively increasing the D2D link’s CH (from 1 to 8) and CRD (from 8 to 128) parameters on ControlPULPlet’s area in GE. A GE represents the area of a two-input, minimum-strength NAND gate. The manager domain SPMs and PMCA dominate the area cost, accounting for nearly 60 % of the system. The link area overhead at fixed flow control credits — dashed red lines referring to the right y-axis — increases approximately linearly, which is expected due to a linear increase in the number of channels. We observe that the most performant configuration in terms of attainable bus utilization (i.e., $CH = 8$ and $CRD = 128$, Section III-A) is lightweight, incurring just 2.9 % area overhead in-system.

Fig. 11 and Fig. 14 highlight the approximate location of Kairos main components and their relative size in the fabricated chip, respectively. The IO pads are on the sides of the chip due to the QFN package. The memory system still dominates the overall area, while the minimal configuration of the link ($CH = 1$, $LN = 8$) incurs 1 % area overhead. The RT mid-end integrated into both system and IO DMA engines adds a minimal area overhead of 2 kGE compared to a vanilla DMA, primarily due to the additional configuration registers

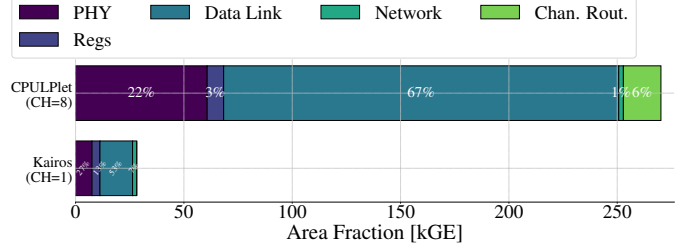


Fig. 15: D2D link area breakdown in ControlPULPlet ($CH = 8$, $CRD = 128$), and the Kairos chip demonstrator ($CH = 1$, $CRD = 8$).

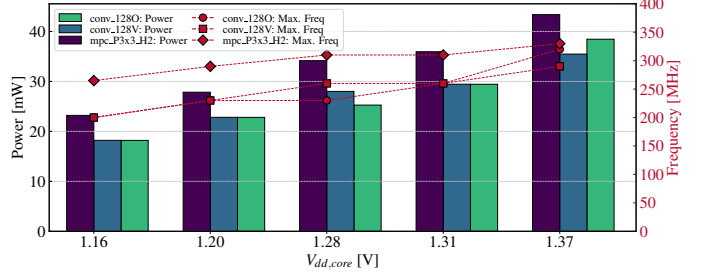


Fig. 16: Kairos power at maximum frequency and varying $V_{dd,core}$ for some relevant benchmarks.

and period counters. Similarly, the fast interrupt handling features impact just 10 % on the area of the CV32RT core.

Figure 15 presents a detailed area breakdown of the D2D link components in ControlPULPlet (top) and the Kairos demonstrator (bottom). In the former, the control flow FIFO occupies more than 60 % of the D2D link area. As the number of channels increases, the PHY’s area contribution starts dominating the D2D link. The size of a single PHY is independent of the flow control FIFO and is particularly lightweight at only 7.6 kGE per channel.

Power Consumption:

a) System Level: To assess Kairos’ power consumption, we select two representative scenarios with varying computational and memory demands (Fig. 16). The `conv_128` benchmark performs a 32 b integer convolution on a 128×128 matrix using a 5×5 filter. We evaluate a vanilla version (`conv_128V`) and an optimized one with SIMD, post-increment load/store, and loop unrolling (`conv_128O`). The `mpc_P3x3_H2` is that described in Section III-B. Figure 16 shows the power consumption (left axis, in black) of the chip at various core voltages $V_{dd,core}$ around the nominal $V_{dd,core}=1.2$ V. For each operating voltage, we find and report the maximum operating frequency (right axis in red). At the nominal 1.2 V, Kairos can achieve frequencies up to 290 MHz, while maintaining a power envelope under 30 mW. A cross-comparison with SoA is provided in the following Section IV. The D2D link accounts for only 1.2 % of total power in silicon-calibrated post-layout simulations using memory-bound synthetic tests.

b) D2D Link: The energy consumption per transferred bit of the D2D interface is affected by two components: one on-chip, due to the D2D microarchitecture, and one off-chip, due to PCB trace length and IO voltage. With D2D interface, we intend the whole network, data link, and PHY modules.

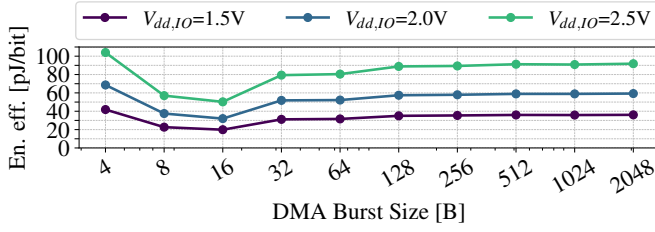


Fig. 17: D2D energy efficiency in Kairos at different $V_{dd,IO}$ and DMA burst lengths, measured using the standalone board.

We evaluate the first component with the testbench framework shown in Fig. 8, which provides fine-grained internal energy estimates within the chip, isolating the D2D link from the rest of the SoC through silicon-calibrated post-layout simulations of ControlPULPlet. The second component is assessed with the manufactured board, as this setup accounts for the impact of I/O voltage and PCB track length between the two chip instances. In both cases, we use DMA-operated transfers to maximize bus utilization, as in Section III-A. Silicon-calibrated post-layout simulations of the chip yield a total internal energy-per-bit of 1.3 pJ/b at nominal $V_{dd,core}=1.2$ V, including network, data link, and physical layers. The PHY accounts for roughly half of this (0.62 pJ/b), with the remainder spent on AXI4-to-AXIS conversion and flow control logic. Figure 17 reports the energy-per-bit across three $V_{dd,IO}$ values, from the minimum functional 1.5 V to the nominal 2.5 V, at varying DMA burst sizes. The energy is minimized at 16 B, matching the data transferred per cycle in DDR mode ($CH = 1$, $LN = 8$). Transfers of 4 B are inefficient, as they use only half of the DMA bus width (8 B). For burst sizes from 32 B to 2 KiB, corresponding to 256 beats and the maximum supported by AXI4, energy increases due to burst fragmentation and flow control FIFO limitations. At $V_{dd,core}=1.5$ V and recalling the average reach of 70.5 mm, the minimum normalized energy is 18.23 pJ/b, highlighting the penalty introduced by I/O voltage and PCB traces compared to internal D2D energy. A 2.5D integration would mitigate this penalty, as interposer tracks are almost two orders of magnitude shorter and offer better electrical properties than standard FR4 PCB traces.

IV. RELATED WORK

In the following, Section IV-A discusses controllers with different acceleration and real-time features, with a focus on their D2D interface, when available. Section IV-B then examines standalone D2D interfaces proposed by prior works.

A. Programmable Hardware Controllers

We focus on *programmable* controllers, which address the limited flexibility of fixed-function controllers [2], [31]. Programmable controllers are classified as (i) single-core programmable, (ii) multi-core programmable, and (iii) heterogeneous multi-core controllers with DSAs. Table I highlights the relevant SoA in this category. The table groups controllers by D2D interface support.

a) Single-core Programmable Controllers: Single-core programmable controllers like STMicroelectronics' 32 b STM32 series (Fig. 2a) support real-time applications with accelerated context switching, consuming less than 150 mW at 500 MHz [21]. Similarly, AURIX TriCore TC2xx series provides hardware-assisted context switching with 10-16 clock cycles interrupt response time and 156-162 clock cycles context switching [22], consuming 300 mW at just 130 MHz. Our design outperforms TriCore in interrupt latency and context switching (both $1.6\times$ faster) with similar power consumption.

On-chip single-core controllers for CPU DVFS and SoC management include Intel's power control unit (PCU) [23], IBM's on-chip controller (OCC) [24], Arm's system control processor (SCP) [5], and AMD's system management unit (SMU) [17], all based on 32 b commercial processors. These controllers implement simple PID control policies with control periods of 0.25 ms to 1 ms, aligning favorably with ControlPULP's capabilities. The SMU uniquely integrates a chiplet-based D2D interface via AMD's Infinity Fabric on Package (IFOP). IFOP comprises a scalable data and control fabric (SDF and SCF, respectively). Online CPU DVFS is managed through the SCP with a 1 ms-period PID policy, facilitating communication from the SMU, located within the IO die (IOD) chiplet, to the compute chiplets housing high-performance Zen cores. In AMD's Rome [28], IFOP achieves 2 pJ/b and 440 GB/s at 1.2 V on a 12 nm passive interposer, though control and data planes likely have different bandwidth needs. A similar chiplet-compatible D2D demonstrator using an OpenRISC microcontroller in 16 nm achieves 2 Gb/s per pin with 1.5 pJ/b at 1.2 V [29]. While these controllers prioritize deterministic execution, fast context switching, and efficient D2D control interfaces, they lack the computational power required by advanced control algorithms.

b) Multi-core Controllers: Multi-core controllers address this computational gap. The six-core AURIX TC29x [25] and ASPEED's AST2600, a common Baseboard Management Controller [26], demonstrate increased processing capability, reflected in their high power consumption, between 1.5 W to 2 W. However, general-purpose cores result in high silicon cost and lower energy efficiency for specialized workloads.

c) Heterogeneous Multi-core Controllers: To improve efficiency, heterogeneous multi-core controllers integrate DSAs. ControlPULP combines a 32 b embedded core with an 8-core tightly-coupled PMCA, balancing flexibility, performance, and efficiency for real-time control applications [3]. Similarly, AURIX TC4x series integrates a 6-core high-end controller with diverse accelerators for AI-based model predictive and model adaptive control [27]. Register banking enables fast interrupt response clock cycles and context switching, key properties retained from its predecessors. Increased acceleration and performance incurs additional power consumption costs than the low-end TC2x series, about 2.5 W. Most multi-core and heterogeneous controllers are available as standalone chips or soft intellectual property (IP) blocks for on-chip integration, but few support chiplet-compatible D2D interfaces. A notable exception is the 96-core demonstrator by Vivet et al., which integrates a power management controller including switched-capacitor voltage regulators (SCVRs), one for each

TABLE I: Comparison of programmable controller classes. We highlight several metrics of the controller. The autonomous DMA is not highlighted, as it is unique to our design.

Controller	Class	Applic.	DSA Integr.	D2D Interf.	Fast Interr.	Tech [nm]	Max. Freq. [MHz]	Peak Power [mW]	D2D					
									Prot.	#Links	#Wires/Link	Peak BW [Gb/s]	Reach [mm]	En. eff. [pJ/b]
Controllers for 2D integration with simple on-chip or off-chip interfaces														
STM32 [21]	1-core	IoT	✓	✗	✗	28	24-480	66-132 @3.3 V	-	-	-	-	-	-
TC21XL [22]	1-core	automotive	✓	✗	✗	65	133	290 @3.3 V	-	-	-	-	-	-
PCU [23]	1-core, FSMs	CPU DVFS	✗	✗	n.a.	a.	n.a.	n.a.	-	-	-	-	-	-
OCC [24]	1-core	CPU DVFS	✗	✗	✗	a.	<266-658	n.a.	-	-	-	-	-	-
SCP [5]	1-core	CPU DVFS	✗	✗	✓	a.	<400	n.a.	-	-	-	-	-	-
TC29x [25]	3-cores	automotive	✓	✗	✓	-	<400	1697 @3.3 V	-	-	-	-	-	-
AST2600 [26]	2-cores	server mngmnt	✗	✗	✗	28	1000, Cort. A 200, Cort. M	> 2000 @1.8-3.3 V	-	-	-	-	-	-
TC4x [27]	6-cores DSAs	automotive	✓	✗	✓	28	500	2240-2501 @3.3 V	-	-	-	-	-	-
ControlPULP [3]	1-core PMCA	automotive	✓	✗	✓	d22	d500	n.a.	-	-	-	-	-	-
Controllers for 2.5D integration with die-to-die interfaces														
AMD SMU [17], [28]	1-core	CPU DVFS	✗	✓	✗	b12	n.a.	n.a.	IFOP	c8	n.a.	c3520 @2 GHz	n.a.	c2 @1.2 V
Liu et al. [29]	1-core	n.a.	✗	✓	✗	16	500, OpenRISC 1000, D2D	n.a.	AIB-like	3	96	2 (per pin) @1 GHz	<2	1.48 @1.2 V
Vivet et al. [30]	n.a.	CPU DVFS	n.a.	✓	n.a.	n.a.	1200	e1160	3D Plug	6+8+1	12	3152 @1.1 GHz	1.5-1.8	0.75 @1.2 V
ControlPULPlet (ours)	1-core PMCA	n.a.	✓	✓	✓	65	f290	f30 / g210	custom	f1 – h8	16+2	h>51 @200 MHz	<70.5	i1.3 – f11.7 @1.2 V

^a soft IP not tied to standalone chip ^b IO die (IOD) ^c from AMD Rome; we report Infinity Fabric numbers, exact SCF values are unavailable
^d soft IP not tied to standalone chip, reported post-synthesis estimates ^e one SCVR
90% of the on-chip control interface requirements; optimizable at additional area cost ^f internal energy estimated with silicon-calibrated post-layout simulation ^g considering both manager and PMCA domains ^h peak with CH=8, CRD=128, scaled from V_{dd,IO}=1.5 V (measured on Kairos demonstrator)

^a soft IP not tied to standalone chip ^b IO die (IOD) ^c from AMD Rome; we report Infinity Fabric numbers, exact SCF values are unavailable ^d soft IP not tied to standalone chip, reported post-synthesis estimates ^e one SCVR ^f Kairos demonstrator @ $V_{dd,core}=1.2$ V, $V_{dd,IO}=1.5$ V ^g considering both manager and PMCA domains ^h peak with $CH=8$, $CRD=128$, 90% of the on-chip control interface requirements; optimizable at additional area cost ⁱ internal energy estimated with silicon-calibrated post-layout simulation ^j scaled from $V_{dd,IO}=1.5$ V (measured on Kairos demonstrator)

TABLE II: Comparison of standalone D2D Interfaces. We highlight several metrics of each interface. A and D refer to analog and digital, respectively.

D2D Interface	Tech [nm]	On-chip Protocol	Design	Reach [mm]	Peak BW [Gb/s]	Area [kGE]	Energy [pJ/b]	#Wires /Link
Kuttappa et al. [32]	16	aAXI (36 b)	A/D	1.2	b18 @1 GHz	n.a.	c0.85	18+8
Melek et al. (UCIe) [33]	3	n.a.	A/D	1.4	2048 @8 GHz	n.a.	0.29 @0.45 V	64+4
BoW [20]	65-5	PCIe, MAC PIPE/LPIF	D	10	d5-8 @2.5-4 GHz	n.a.	<1 @0.7-0.9 V	16+2
Lin et al. (LIPINCON) [34]	7	Mesh (1968 b)	A/D	0.5	2560 @4GHz	e18420	0.56 @0.3 V	40+6
GRS [35]	16	n.a.	A/D	80	d25 @12.5GHz	589.9	1.17 @0.3 V	8+1
Li et al. [36]	Kintek-7 FPGA	n.a. (64 b)	D	n.a.	8.3 @250 MHz	n.a.	n.a.	32+1+1
Ours	65	AXI4 (64b)	D	f70.5	51 @200 MHz	#28.2/h270.2 (7.6 one PHY)	11.7 (1.3 int.) @1.2 V	16+2

^a The exact AXI protocol (AXI3 or AXI4) not specified ^b Aggregate BW of one cluster only ^c Operational voltage is not specified ^d Per pin ^e one channel (implemented 2 channels per chiplet) ^f Reach based on the average trace length of the PCB shown in Fig. 12; other works refer to interposer-based reach ^g Network, data, and PHY for the Kairos config. $CH = 1$, $LN = 8$ ^h Network, data, and PHY for the peak BW config. $CH = 8$, $LN = 8$

compute chiplet, on an active silicon interposer [30].

B. D2D Interfaces

Table II compares industrial and academic D2D protocols. While energy-per-bit is difficult to compare due to differing technology nodes and voltages, peak bandwidth can be scaled assuming higher frequencies, though still bounded by the frontend bus width. Area is reported in gate equivalents, normalized to a minimum-strength NAND gate, making it technology-agnostic. UCIe [33], BoW [20], and LIPINCON over CoWoS [34] support widely used frontend standards, such as PCIe and CXL. The standalone D2D interfaces and protocols surveyed in Table II are specifically optimized for high-throughput communication across the data plane of the chiplet, driving the design toward high-frequency operation

(in the multi-GHz range) and the scaling out of individual link instances. Table II presents the number of wires per link as a normalized figure of merit for this purpose. For example, GRS [35] achieves 25 Gb/s per pin over an 80 mm reach on a silicon interposer, operating at a high frequency of 12.5 GHz. Similarly, LIPINCON [34] integrates 1968 parallel bits, while in [33], Cadence proposes a UCIe-compatible D2D interface with 64 parallel data wires across 8 links delivering 2048 Gb/s at 8 GHz. These implementations contrast with the 64 b AXI4 frontend used in this work for the control plane interface, where high bandwidth and speed are not primary requirements. However, because of its flexibility, our D2D design can be readily scaled to meet the demands of a wider data bus for data-intensive applications. Similar to our work, Intel's design in [32] features a D2D interface with an

AXI frontend, and a 36 b data bus. The mixed analog/digital PHY is integrated into a 14-cluster system on chip (SoC) for media and ML applications, using 9 data wires per cluster to deliver 18 Gb/s at 1 GHz per cluster. Though currently dataplane-focused, these high-bandwidth links enable future D2D communication in complex distributed control systems, making them increasingly relevant for control-plane use. In academia, Li et al. [36] propose a custom, parallel D2D interface achieving 8.3 Gb/s at 250 MHz. The microarchitecture only supports a fixed 32 parallel data lanes with a 64b buffer FIFO used for protocol conversion. Moreover, the D2D physical implementation assessment is limited to FPGA mapping without silicon prototyping, which prevents accurate power and area estimates.

Our D2D design stands out for its lightweight area overhead, even when configured for peak throughput ($CH = 8$, $LN = 8$ for a data bus of 64 b). As shown in Table II, it achieves a smaller die size than PHY-only reported implementations in more advanced technology nodes, such as [35] ($2.2\times$) and [34] ($136\times$), while also incorporating the data link and network layers. Furthermore, the link achieves higher throughput compared to designs with similar microarchitecture and operating frequency, e.g., [36], which reports $6\times$ less bandwidth while doubling the number of wires per link. At iso-frequency, our interface achieves superior peak bandwidth, e.g., outperforming the recent [32] by $14\times$, thanks to the high bus utilization enabled by the D2D design, despite other works using more advanced technology nodes. The energy efficiency of our silicon prototype is negatively affected by the flat QFN package and the lack of an interposer as substrate, leading to PCB-induced overhead (PCB track parasitic). However, cycle-accurate simulations provide high observability of the inner D2D circuitry, enabling silicon-calibrated measurement of its internal energy (1.3 pJ/b), a lower bound independent from the length and parasitics of the off-die wires. The inner D2D energy is comparable with leading academic and industry designs at the same voltage, e.g., [29] (1.48 pJ/b) and the AMD SMU [17] (2 pJ/b). Moreover, since energy-per-bit scales with the square of the operating voltage, a more advanced technology node enabling lower voltages could reduce our energy-per-bit below 1 pJ/b, proving it competitive with the surveyed works.

V. CONCLUSION

To meet the demands of real-time control algorithms with increasing performance requirements and the trend toward SiP and chiplet integration technology, we introduce ControlPULPlet, an open-source, real-time, heterogeneous multi-core RISC-V controller. It features a 32 b CV32RT core for fast and deterministic interrupt management, a specialized DMA for real-time data transfer, and a tightly-coupled PMCA for compute-intensive control algorithm acceleration. A flexible AXI4-compatible D2D link supports both inter-chiplet and on-chip communication. Operating at 1.2 V, Kairos, ControlPULPlet's silicon demonstrator in 65nm CMOS, peaks at 290 MHz within 30 mW power envelope during intensive control workloads. The D2D link enables off-die access at

11.7 pJ/b at 1.2 V IO voltage, with only 1.3 pJ/b internal energy, attaining duplex peak transfer rates of 51 Gb/s at 200 MHz, 2.9% and 1.2% area and power penalties, and minimal performance degradation on periodic control policies compared to its on-chip counterpart.

REFERENCES

- [1] F. Rehm, J. Seitter, J.-P. Larsson, S. Saidi, G. Stea, R. Zippo, D. Ziegenbein, M. Andreozzi, and A. Hamann, "The road towards predictable automotive high - performance platforms," in *2021 Des., Automat. & Test in Eur. Conf. & Exhib. (DATE)*, 2021, pp. 1915–1924.
- [2] H. Ren, K. Sahoo, Z. Guo, R. Pugazhendhi, Z. Wong, T. Xiang, T. S. Fisher, and S. S. Iyer, "Heterogeneous power delivery for large chiplet-based systems using integrated gan/si-interconnect fabric with sub-10 um bond pitch," in *2023 Int. Electron Devices Meeting (IEDM)*, 2023, pp. 1–4.
- [3] A. Ottaviano, R. Balas, G. Bambini, A. D. Vecchio, M. Ciani, D. Rossi, L. Benini, and A. Bartolini, "Controlpulp: A risc-v on-chip parallel power controller for many-core hpc processors with fpga-based hardware-in-the-loop power and thermal emulation," *Int. J. of Parallel Program.*, vol. 52, no. 1, pp. 93–123, apr 2024.
- [4] X. Li, L. Chen, S. Chen, F. Jiang, C. Li, W. Zhang, and J. Xu, "Deep reinforcement learning-based power management for chiplet-based multicore systems," *IEEE Trans. on Very Large Scale Integration (VLSI) Systems*, vol. 32, no. 9, pp. 1726–1739, 2024.
- [5] Arm, "Power control system architecture," <https://developer.arm.com/documentation/den0050/d/?lang=en>, 2023, accessed: 2025-02-05.
- [6] A. Esper, G. Nelissen, V. Nelis, and E. Tovar, "An industrial view on the common academic understanding of mixed-criticality systems," *Real-Time Syst.*, vol. 54, 07 2018.
- [7] D. Mishra, V. Arora, L. Nguyen, S. Iriguchi, H. Sada, L. Clemente, S. Lim, H. Lin, A. Lohia, S. Gurrum, J. Sauser, and S. Spencer, "Packaging innovations for high voltage (hv) gan technology," in *2017 IEEE 67th Electron. Compon. and Technol. Conf. (ECTC)*, 2017, pp. 1480–1484.
- [8] S. Mirabbasi, L. C. Fujino, and K. C. Smith, "Through the looking glass—the 2023 edition: Trends in solid-state circuits from isccc," *IEEE Solid-State Circ. Mag.*, vol. 15, no. 1, pp. 45–62, 2023.
- [9] D. D. Sharma, G. Pasdast, S. Tiagaraj, and K. Aygün, "High-performance, power-efficient three-dimensional system-in-package designs with universal chiplet interconnect express," *Nature Electronics*, vol. 7, no. 3, pp. 244–254, 2024.
- [10] P. Iff, M. Besta, M. Cavalcante, T. Fischer, L. Benini, and T. Hoefler, "Hexamesh: Scaling to hundreds of chiplets with an optimized chiplet arrangement," in *2023 60th ACM/IEEE Des. Automat. Conf. (DAC)*, 2023, pp. 1–6.
- [11] S. Naffziger, N. Beck, T. Burd, K. Lepak, G. H. Loh, M. Subramony, and S. White, "Pioneering chiplet technology and design for the amd epyc™ and ryzen™ processor families : Industrial product," in *2021 ACM/IEEE 48th Annu. Int. Symp. on Comput. Architecture (ISCA)*, 2021, pp. 57–70.
- [12] G. H. Loh, S. Naffziger, and K. Lepak, "Understanding chiplets today to anticipate future integration opportunities and limits," in *2021 Des., Automat. & Test in Europe Conf. & Exhib. (DATE)*, 2021, pp. 142–145.
- [13] A. Kannan, N. E. Jerger, and G. H. Loh, "Enabling interposer-based disintegration of multi-core processors," in *2015 48th Annu. IEEE/ACM Int. Symp. on Microarchitecture (MICRO)*, 2015, pp. 546–558.
- [14] R. Balas, A. Ottaviano, and L. Benini, "Cv32rt: Enabling fast interrupt and context switching for risc-v microcontrollers," *IEEE Trans. on Very Large Scale Integration (VLSI) Systems*, vol. 32, no. 6, pp. 1032–1044, 2024.
- [15] T. Benz, M. Rogenmoser, P. Scheffler, S. Riedel, A. Ottaviano, A. Kurth, T. Hoefler, and L. Benini, "A high-performance, energy-efficient modular dma engine architecture," *IEEE Trans. on Comput.*, vol. 73, no. 1, pp. 263–277, 2024.
- [16] Intel, "Configuring power management functionalities in a processor," U.S. Patent US8984313B2, March 2015.
- [17] T. Burd, N. Beck, S. White, M. Paraschou, N. Kalyanasundharam, G. Donley, A. Smith, L. Hewitt, and S. Naffziger, "'Zeppelin': An SoC for Multipich Architectures," *IEEE J. of Solid-State Circuits*, vol. 54, no. 1, pp. 133–143, 2019.
- [18] Arm, "AMBA AXI and ACE Protocol Specification AXI3, AXI4, and AXI4-Lite ACE and ACE-Lite," <https://developer.arm.com/documentation/ih0022/latest/>, 2023, version J.

- [19] G. Bambini, A. Ottaviano, C. Conficoni, A. Tilli, L. Benini, and A. Bartolini, "Modeling and controlling many-core hpc processors: An alternative to pid and moving average algorithms," *ACM Trans. Auton. Adapt. Syst.*, Sep. 2024. [Online]. Available: <https://doi.org/10.1145/3694687>
- [20] S. Ardalani, H. Cirit, R. Farjad, M. Kuemerle, K. Poulton, S. Subramanian, and B. Vinnakota, "Bunch of wires: An open die-to-die interface," in *2020 IEEE Symp. on High-Perform. Interconnects (HOTI)*, 2020, pp. 9–16.
- [21] STMicroelectronics, *STM32F042F6 Microcontroller*, STMicroelectronics, 2024, accessed: 2025-02-05. [Online]. Available: <https://www.st.com/en/microcontrollers-microprocessors/stm32f042f6.html>
- [22] Infineon, *AURIX Family - TC21XL*, Infineon, 2024, accessed: 2025-02-05. [Online]. Available: <https://www.infineon.com/cms/en/product/microcontroller/32-bit-tricore-microcontroller/32-bit-tricore-aurix-tc2xx/>
- [23] R. Schöne, T. Ilsche, M. Bielert, A. Gocht, and D. Hackenberg, "Energy efficiency features of the intel skylake-sp processor and their impact on performance," in *2019 Int. Conf. on High Perform. Comput. & Simul. (HPCS)*, 2019, pp. 399–406.
- [24] T. Rosedahl, M. Broyles, C. Lefurgy, B. Christensen, and W. Feng, "Power/Performance Controlling Techniques in OpenPOWER," in *High Perform. Comput.*, J. M. Kunkel, R. Yokota, M. Taufer, and J. Shalf, Eds. Springer Int. Publishing, 2017, pp. 275–289.
- [25] Infineon, *AURIX Family - TC29x*, Infineon, 2024, accessed: 2025-02-05. [Online]. Available: <https://www.infineon.com/cms/en/product/microcontroller/32-bit-tricore-microcontroller/32-bit-tricore-aurix-tc2xx/>
- [26] ASPEED, *AST2600*, ASPEED, 2024, accessed: 2025-02-05. [Online]. Available: https://www.aspeedtech.com/server_ast2600/
- [27] Infineon, *AURIX Family - TC4x*, Infineon, 2024, accessed: 2025-02-05. [Online]. Available: <https://www.infineon.com/cms/en/product/microcontroller/32-bit-tricore-microcontroller/32-bit-tricore-aurix-tc4x/>
- [28] S. Naffziger, K. Lepak, M. Paraschou, and M. Subramony, "2.2 and chiplet architecture for high-performance server and desktop products," in *2020 IEEE Int. Solid-State Circuits Conf. - (ISSCC)*, 2020, pp. 44–45.
- [29] C. Liu, J. Botimer, and Z. Zhang, "A 256gb/s/mm-shoreline aib-compatible 16nm finfet cmos chiplet for 2.5d integration with stratix 10 fpga on emib and tiling on silicon interposer," in *2021 IEEE Custom Integr. Circuits Conf. (CICC)*, 2021, pp. 1–2.
- [30] P. Vivet, E. Guthmuller, Y. Thonnart, G. Pillonnet, C. Fuguet, I. Miropanades, G. Moritz, J. Durupt, C. Bernard, D. Varreau, J. Pontes, S. Thuries, D. Coriat, M. Harrand, D. Dutoit, D. Lattard, L. Arnaud, J. Charbonnier, P. Coudrain, A. Garnier, F. Berger, A. Gueugnot, A. Greiner, Q. L. Meunier, A. Farcy, A. Arriordaz, S. Chéramy, and F. Clermidy, "Intact: A 96-core processor with six chiplets 3d-stacked on an active interposer with distributed interconnects and integrated power management," *IEEE J. of Solid-State Circ.*, vol. 56, no. 1, pp. 79–97, 2021.
- [31] Y. K. Cherivirala and D. D. Wentzloff, "A capacitor-less digital ldo regulator with synthesizable pid controller achieving 99.75% efficiency and 93.3-ps response time in 65 nm," *IEEE Trans. on Circ. and Sys. II: Express Briefs*, vol. 70, no. 5, pp. 1769–1773, 2023.
- [32] R. Kuttappa, J. Sundaram, S. R. Srinivasa, P. Aseron, G. Murali, V. Honkote, P. Budhkar, D. Kurian, R. Kalim, T. P. Thomas, A. Srinivasan, and T. Karnik, "A high-performance passive base system for distributed ai/media acceleration," in *2025 IEEE Custom Integr. Circuits Conf. (CICC)*, 2025, pp. 1–6.
- [33] D. T. Melek, R. Navinkumar, J. Vandersand, P. Sarkar, B. Prakash, A. Leuciuc, K. Geary, S. Ma, C. M. Mehta, S. Jain, B. Bothra, P. Sabharwal, R. Vaish, K. Bhanushali, Y. Ding, C. Frost, J. Annunziata, K. Sadhu, D. Kyritsis, J. Bostak, M. Li, S. Williams, and K. Chang, "A 0.29pj/b 5.27tb/s/mm ucie advanced package link in 3nm finfet with 2.5d cowos packaging," in *2025 IEEE Int. Solid-State Circuits Conf. - (ISSCC)*, vol. 68, 2025, pp. 590–592.
- [34] M.-S. Lin, T.-C. Huang, C.-C. Tsai, K.-H. Tam, K. C.-H. Hsieh, C.-F. Chen, W.-H. Huang, C.-W. Hu, Y.-C. Chen, S. K. Goel, C.-M. Fu, S. Rusu, C.-C. Li, S.-Y. Yang, M. Wong, S.-C. Yang, and F. Lee, "A 7-nm 4-ghz arm¹-core-based cowos¹ chiplet design for high-performance computing," *IEEE J. of Solid-State Circuits*, vol. 55, no. 4, pp. 956–966, 2020.
- [35] J. W. Poulton, J. M. Wilson, W. J. Turner, B. Zimmer, X. Chen, S. S. Kudva, S. Song, S. G. Tell, N. Nedovic, W. Zhao, S. R. Sudhakaran, C. T. Gray, and W. J. Dally, "A 1.17-pj/b, 25-gb/s/pin ground-referenced single-ended serial link for off- and on-package communication using a process- and temperature-adaptive voltage regulator," *IEEE J. of Solid-State Circuits*, vol. 54, no. 1, pp. 43–54, 2019.
- [36] S. Li, Y. Wang, C. Feng, and H. Wang, "Hardware architecture of the universal high-speed interconnection chiplet for chiplet integration," in *2024 9th Int. Conf. on Comput. and Commun. Syst. (ICCCS)*, 2024, pp. 1083–1087.



Alessandro Ottaviano (Graduate Student Member, IEEE) received the B.Sc. in Physical Engineering from Politecnico di Torino, Italy, and the M.Sc. in Electrical Engineering as a joint degree between Politecnico di Torino, Grenoble INP-Phelma and EPFL Lausanne, in 2018 and 2020 respectively. He is currently pursuing a Ph.D. degree in the Digital Circuits and Systems group of Prof. Benini. His research interests include real-time and predictable computing systems and energy-efficient processor architecture.



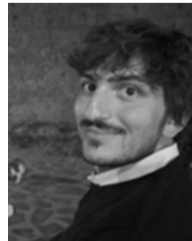
Robert Balas (Graduate Student Member, IEEE) received his B.Sc. and M.Sc. degrees in electrical engineering and information technology from ETH Zurich in 2015 and 2017, respectively. He is currently pursuing a Ph.D. degree in the Digital Circuits and Systems group of Prof. Benini. His research interests include real-time computing, compilers, and operating-systems.



Tim Fischer received his BSc and MSc in "Electrical Engineering and Information Technology" from the Swiss Federal Institute of Technology Zurich (ETHZ), Switzerland, in 2018 and 2021, respectively. He is currently pursuing a Ph.D. degree at ETH Zurich in the Digital Circuits and Systems group led by Prof. Luca Benini. His research interests include scalable and energy-efficient interconnects for both on-chip and off-chip communication.



Thomas Benz (Graduate Student Member, IEEE) received his B.Sc. and M.Sc. degrees in electrical engineering and information technology from ETH Zurich in 2018 and 2020, respectively. He is currently pursuing a Ph.D. degree in the Digital Circuits and Systems group of Prof. Benini. His research interests include energy-efficient high-performance computer architectures, memory interconnects, data movement, and the design of ASICs.



Andrea Bartolini (Member, IEEE) received the Ph.D. degree from the University of Bologna, Bologna, Italy, in 2013. He is an Associate Professor with the Department of Electrical, Electronic and Information Engineering Guglielmo Marconi, University of Bologna, Bologna, Italy. He has published more than 120 papers in peer-reviewed international journals and conferences and several book chapters with focus on dynamic resource management, ranging from embedded to large-scale HPC systems.



Luca Benini (Fellow, IEEE) holds the chair of digital Circuits and systems at ETHZ and is Full Professor at the Università di Bologna. He received a PhD from Stanford University. His research interests are energy-efficient parallel computing systems, smart sensing micro-systems, and machine learning hardware. He is a Fellow of the IEEE, of the ACM, a member of the Academia Europaea, and of the Italian Academy of Engineering and Technology.